Article

Cell

# Molecular Structure of the Human CFTR Ion Channel

## Graphical Abstract

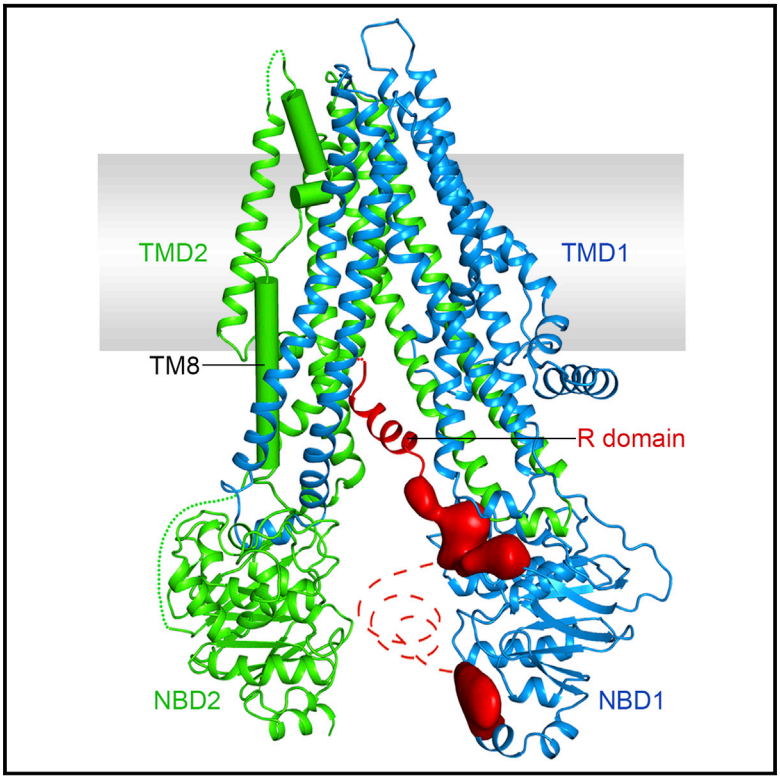


## Authors

Fangyu Liu, Zhe Zhang, László Csanády, David C. Gadsby, Jue Chen

## Correspondence

juechen@rockefeller.edu

## In Brief

Molecular structure of human CFTR determined in the dephosphorylated, ATP-free conformation provides insights on the structural basis for its channel activity.

## Highlights

- Molecular structure of human CFTR in the dephosphorylated, ATP-free form
- Correlation between CFTR channel gating cycle and ATP hydrolysis rates
- Identification of a structure feature distinguishing CFTR from other ABC transporters

Liu et al., 2017, Cell *169*, 85–95
March 23, 2017 © 2017 Elsevier Inc.
http://dx.doi.org/10.1016/j.cell.2017.02.024

CellPress

Cell

# Molecular Structure of the Human CFTR Ion Channel

Fangyu Liu,[1,2,6] Zhe Zhang,[1,3,6] László Csanády,[4] David C. Gadsby,[5] and Jue Chen[1,3,7,*]
[1]Laboratory of Membrane Biophysics and Biology, The Rockefeller University, 1230 York Avenue, New York, NY 10065, USA
[2]Tri-Institutional Training Program in Chemical Biology, The Rockefeller University, 1230 York Avenue, New York, NY 10065, USA
[3]Howard Hughes Medical Institute, 4000 Jones Bridge Road, Chevy Chase, MD 20815, USA
[4]Department of Medical Biochemistry and MTA-SE Ion Channel Research Group, Semmelweis University, Budapest 1094, Hungary
[5]Laboratory of Cardiac/Membrane Physiology, The Rockefeller University, 1230 York Avenue, New York, NY 10065, USA
[6]Co-first author
[7]Lead Contact
*Correspondence: juechen@rockefeller.edu
http://dx.doi.org/10.1016/j.cell.2017.02.024

## SUMMARY

**The cystic fibrosis transmembrane conductance regulator (CFTR) is an ATP-binding cassette (ABC) transporter that uniquely functions as an ion channel. Here, we present a 3.9 Å structure of dephosphorylated human CFTR without nucleotides, determined by electron cryomicroscopy (cryo-EM). Close resemblance of this human CFTR structure to zebrafish CFTR under identical conditions reinforces its relevance for understanding CFTR function. The human CFTR structure reveals a previously unresolved helix belonging to the R domain docked inside the intracellular vestibule, precluding channel opening. By analyzing the sigmoid time course of CFTR current activation, we propose that PKA phosphorylation of the R domain is enabled by its infrequent spontaneous disengagement, which also explains residual ATPase and gating activity of dephosphorylated CFTR. From comparison with MRP1, a feature distinguishing CFTR from all other ABC transporters is the helix-loop transition in transmembrane helix 8, which likely forms the structural basis for CFTR's channel function.**

## INTRODUCTION

Cystic fibrosis (CF) is the most common lethal genetic disorder in populations of Northern European descent, affecting one out of every 2,500 newborns (Boat et al., 1989; Rommens et al., 1989). It is caused by mutations in a single gene, the cystic fibrosis transmembrane conductance regulator (CFTR) (Riordan et al., 1989; Rommens et al., 1989). CFTR belongs to the ATP-binding cassette (ABC) superfamily, but it is unique among ABC proteins in that it functions as an ion channel (Gadsby et al., 2006). Whereas other ABC transporters utilize the chemical energy of ATP hydrolysis to transport substrates against their chemical gradients, CFTR conducts anions down their electrochemical gradient.

A typical ABC transporter consists of two transmembrane domains (TMDs) that form the translocation pathway and two cytoplasmic nucleotide-binding domains (NBDs) that hydrolyze ATP. CFTR contains an additional regulatory (R) domain that must be phosphorylated to allow the channel to open (Cheng et al., 1991). Once the R domain is phosphorylated, ATP binding opens the CFTR channel and ATP hydrolysis closes it (Gunderson and Kopito, 1995). The molecular mechanisms underlying R domain regulation and ATP-dependent gating have been studied for many years, but several key questions remain unanswered.

Recently, we determined the structure of CFTR from zebrafish (Zhang and Chen, 2016). We showed that the ion conduction pathway consists of a large cytosolic vestibule, a narrow transmembrane (TM) tunnel, and a single gate near the extracellular surface. The dephosphorylated regulatory domain, found in the intracellular opening between the two cytosolic halves of the molecule, is positioned to prevent NBD dimerization. However, because only 55% of zebrafish and human CFTR sequence is identical, and because most functional studies were of human CFTR, we reasoned that the structure of human CFTR is essential to directly correlate structure with function.

## RESULTS AND DISCUSSION

### Structural Determination

Full-length human CFTR was overexpressed and purified from human embryonic kidney cells and treated with phosphatase to obtain a homogeneous sample of dephosphorylated protein. Electron cryomicroscopy (cryo-EM) reconstruction was carried out in the absence of nucleotides to an overall resolution of 3.9 Å (Figure S1). The local resolution, estimated by Blocres from the Bsoft package (Heymann and Belnap, 2007), varies from 2.4 Å to 6.0 Å (Figure S1). We built all of the transmembrane helices de novo as the map shows well-defined densities for most of the side chains (Figure S2). High-resolution crystal structures of isolated NBDs were docked into the cryo-EM map and side-chain positions were manually adjusted based on the EM density (Figure S2). A tubular density was clearly visible between the two halves of the molecule; but it lacks side-chain features to establish the amino acid register (Figures S2 and S3). We modeled a short helix likely corresponding to the C-proximal end of the R domain into this density. The final structure, which contains nearly complete atomic models for the lasso, TMD1, TMD2, NBD1, NBD2, and a polyalanine model of residues 825–843, was refined against the EM maps to good

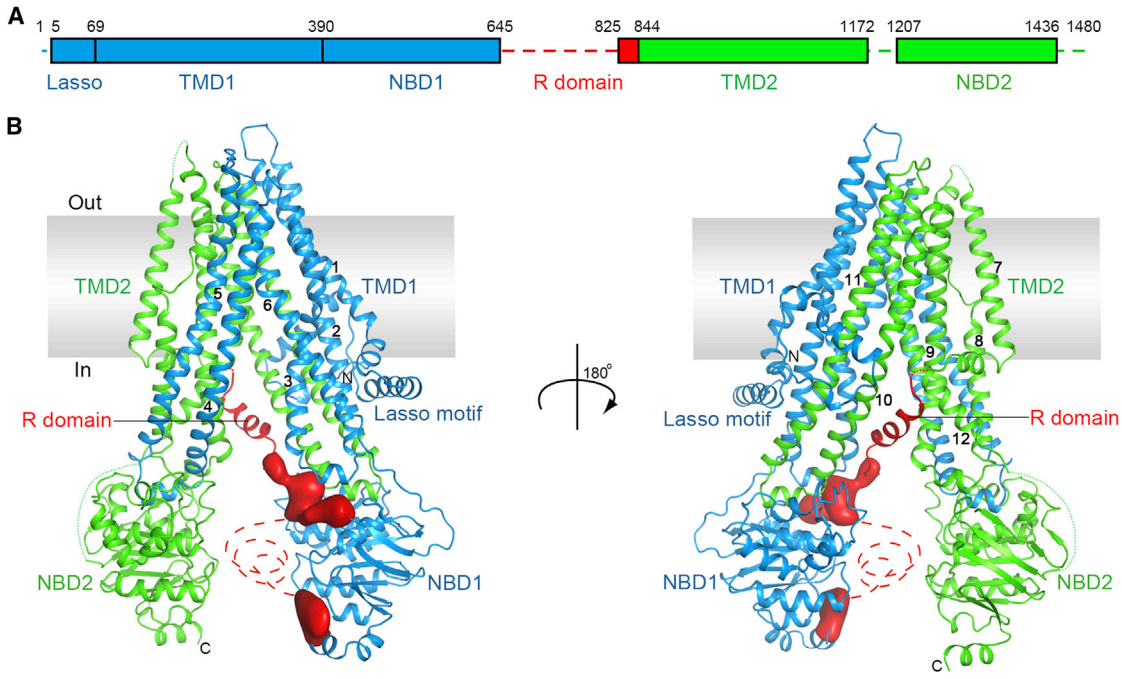


**Figure 1. The Overall Structure of Human CFTR in the Dephosphorylated, ATP-Free Conformation**

(A) The domain structure of CFTR.

(B) Ribbon diagram of two views. The EM densities shown in red correspond to unstructured regions within the R insertion of NBD1 or the R domain. Regions not resolved in the structure are shown as dashed lines for visualization purposes only, they are not meant to imply connectivity or the location of the missing regions.

See also Figures S1–S3 and Table S1.

statistics and excellent stereochemistry (Figures 1 and S1; Table S1).

In this non-phosphorylated, closed-channel conformation, CFTR resembles a typical ABC transporter in its inward-facing conformation (Figure 1). The 12 TM helices in the TMDs pack tightly in the membrane outer leaflet. In the inner leaflet, the helices segregate into two bundles extending ~30 Å into the cytoplasm. The two NBDs, each attached to a cytosolic TM helical bundle, are well separated. The R domain, mostly unstructured, inserts between the cytoplasmic extension of the TMDs and packs along NBD1 in the opening between the two halves of the molecule.

## Structural Comparison of the Two CFTR Orthologs

This structure of human CFTR is very similar to that of the dephosphorylated zebrafish ortholog, evident by the overall root-mean-square deviation (RMSD) of 1.9 Å for 1,062 Cα positions (Figure 2A). Several prominent features of CFTR, including the N-terminal interfacial lasso motif (Figure 2B), the discontinuity of helix TM8 (Figure 2C), and the asymmetric opening of the NBDs (Figure 2D), are conserved in both human and zebrafish orthologs. The positions of functionally important residues, such as the R347/D924 (TM6/TM8) salt-bridge (Figure 2E), the TM6 gating residues F337 and T338 (Figure 2E), and many pore-lining residues (Figure 3) are very similar in both structures.

These structural similarities between human and zebrafish CFTR, given that they possess only 55% sequence identity, have significance. Our observation of closely similar structures in CFTR from two different species offers confidence that both cryo-EM structures represent a functionally informative conformation. Thus, major conclusions reached on the basis of the zebrafish ortholog (Zhang and Chen, 2016), including the construction of the ion-conduction pathway, the separation of the NBDs, the positioning of the R domain, and the structural interpretation of many cystic fibrosis-causing mutations, are now reinforced by the human CFTR structure.

It is quite remarkable that the distances between the two NBDs are so similar in zebrafish and human CFTR (Figure 2D). Many ABC transporters appear to be very flexible in the inward-facing conformation. For example, several crystal structures of the mouse P-glycoprotein display a distribution of distances separating the two NBDs (Ward et al., 2013). Similarly, EM studies of MsbA and P-glycoprotein revealed numerous conformations of both transporters (Frank et al., 2016; Moeller et al., 2015). In stark contrast, we find practically identical conformations and NBD separations in two structures of CFTR from different species, suggesting that the conformational flexibility observed in other ABC transporters is substantially diminished in CFTR. We propose this is due to the presence of the R domain, which in its unphosphorylated state is seen to contact both halves of the molecule (Figure 1).

## Functional Role of Positively Charged Residues

Integral membrane proteins in general contain predominantly hydrophobic residues that form transmembrane segments.

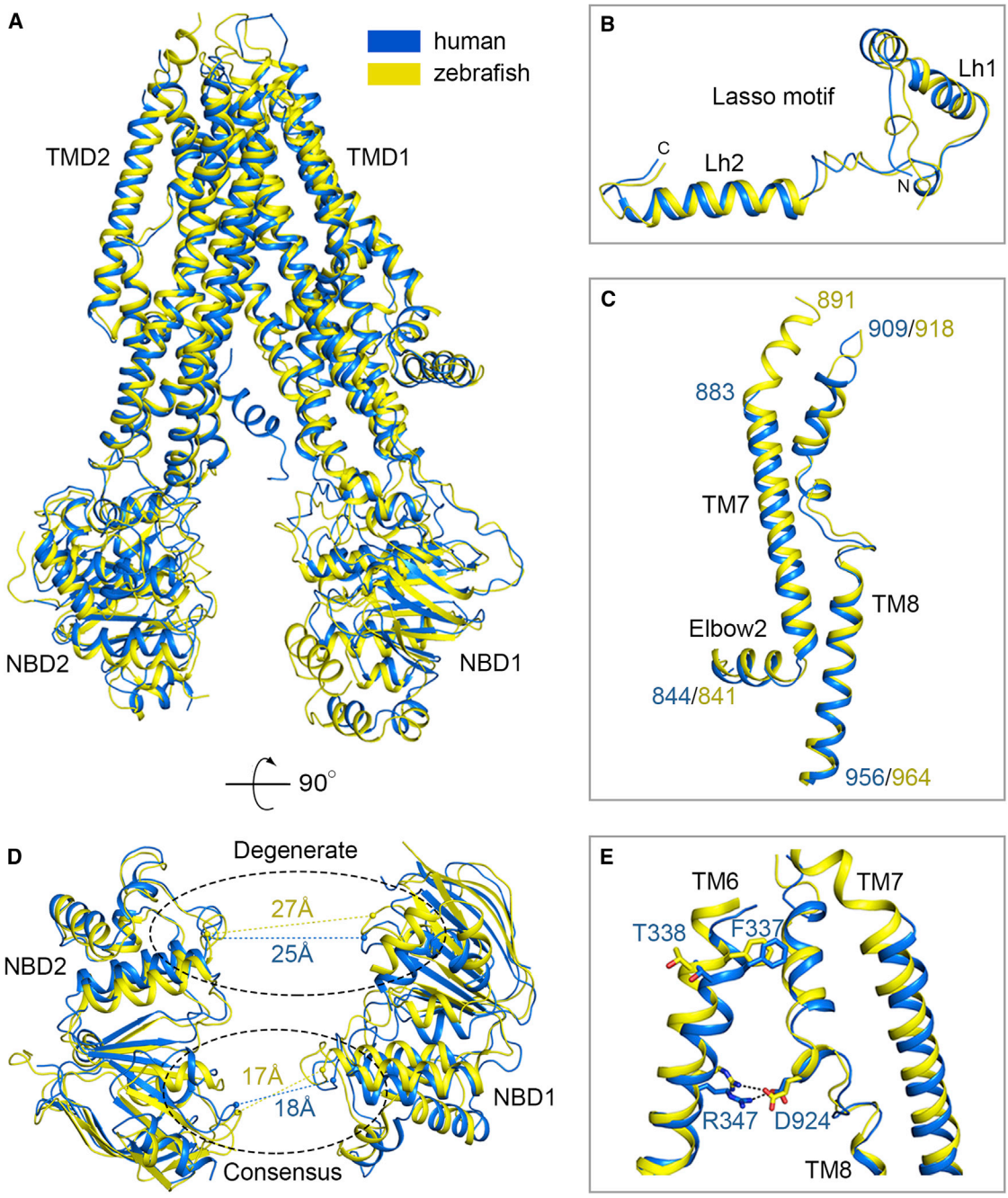


**Figure 2. Structural Comparison of Human and Zebrafish CFTR**

(A) Superposition of the overall structures. Human CFTR is shown in blue, and zebrafish CFTR is in yellow.

(B) Superposition of the lasso motif.

(C) The TM helix 7 in zebrafish CFTR is ten residues longer than that of human CFTR. The residue numbers of human (blue) and zebrafish (yellow) CFTR are indicated.

(D) The asymmetric opening of the NBD interface is conserved in both human and zebrafish CFTR. The distances between the Cα atoms of the conserved glycine in the Walker A motif and the serine in the signature motif are indicated.

(E) Superposition showing the locations of several functionally well-characterized residues.

Positively charged arginine and lysine residues are often found at the cytoplasmic boundaries of the membrane proteins, but are rare within the membrane core or near the extracellular surface. This biased distribution of positively charged residues, the "positive-inside" rule, is important in directing the topology of membrane proteins (Heijne, 1986; Nilsson et al., 2005). CFTR,

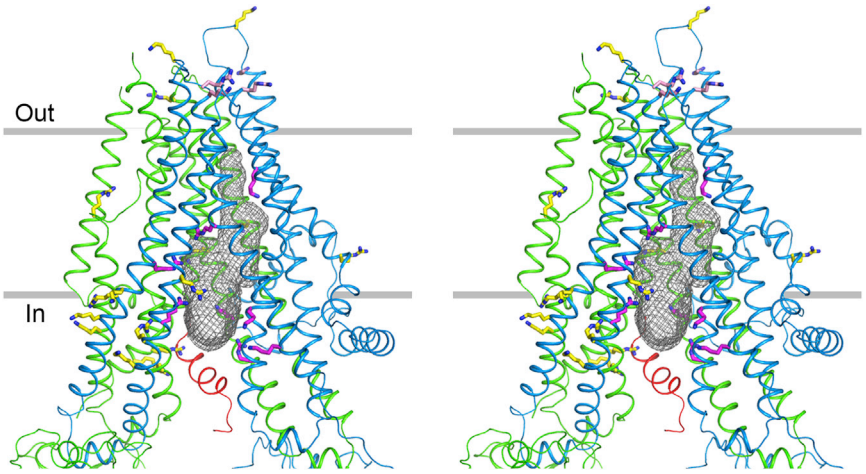


**Figure 3. Stereo View of the Ion-Conduction Pathway**

The pore is shown as a gray mesh. Positively charged residues involved in recruiting extracellular ions are shown in pink, including R104, R117, R334, and K335 (Gong and Linsdell, 2003; Smith et al., 2001; Zhou et al., 2008). Other residues involved in ion conductance are shown in magenta, including K95, K190, R248, R303, R352, K370, K1041, and R1048 (Aubin and Linsdell, 2006; El Hiani and Linsdell, 2015; Ge et al., 2004; Zhou et al., 2007, 2008). Positively charged residues not involved in ion conduction are shown in yellow, including R80, K114, R242, R251, K254, K294, R297, K298, K329, R933, K946, R975, R1030, R1102, R1128, R1162, and R1165 (Aubin and Linsdell, 2006; El Hiani and Linsdell, 2015; Zhang and Hwang, 2015; Zhou et al., 2008).

however, contains a large number of arginines and lysines distributed throughout the TMDs. The functional roles of individual arginine and lysine residues have been studied extensively (Linsdell, 2017). Single amino acid substitution of K95, R104, R117, K190, R248, R303, R334, K335, R352, K370, K1041, and R1048 decreases the single-channel conductance in a charge-dependent manner, suggesting that they play a role in attracting anions into the pore through electrostatic interactions (Aubin and Linsdell, 2006; El Hiani and Linsdell, 2015; Ge et al., 2004; Smith et al., 2001; Zhou et al., 2007, 2008, 2010). Of these residues, R104, R117, R334, and K335 are located in the extracellular region (Figure 3, pink residues). Removing these positive charges leads to inward rectification, consistent with their role in recruiting extracellular anions (Gong and Linsdell, 2003; Smith et al., 2001; Zhou et al., 2008). All other functionally important arginines and lysines are located on the surface of the ion conduction pathway (Figure 3, magenta residues). The side chains of these residues, not engaged in any specific interactions with other parts of the protein in the closed channel, are available to bind anions. In contrast, numerous positively charged residues do not affect anion permeation, including R80, K114, R242, R251, K254, K294, R297, K298, K329, R933, K946, R975, R1030, R1102, R1128, R1162, and R1165 (Aubin and Linsdell, 2006; El Hiani and Linsdell, 2015; Zhang and Hwang, 2015; Zhou et al., 2008); all of these residues are located far from the pore (Figure 3, yellow residues).

Do these positively charged residues contribute to ion selectivity? CFTR is a relatively non-selective anion channel, permitting permeation of many monovalent anions including thiocyanate, nitrate, bromide, chloride, iodide, fluoride, formate, and bicarbonate (Linsdell, 2017). Mutagenesis studies have not identified any particular residue involved in determining the observed lyotropic anion selectivity sequence (Linsdell, 2017). Therefore, it is likely that the selection of anions over cations in CFTR comes from the overall positive charge of the pore (Zhang and Chen, 2016) rather than individual residues or a narrow selectivity filter as seen in K channels (Doyle et al., 1998). Large divalent anions, such as phosphates and sulfates, are not conducted by CFTR. Whether this is due to a narrow region of the ion pathway must await the structure of an open CFTR channel.

## Unphosphorylated R Domain Prevents NBD Dimerization

It has been established that opening of a CFTR channel is strictly coupled to the formation of a closed NBD dimer (Mihályi et al., 2016; Vergani et al., 2005). The location of the unphosphorylated R domain observed in both human (Figure 1) and zebrafish CFTR structures (Zhang and Chen, 2016) is consistent with its inhibitory role (Csanády et al., 2000) by preventing NBD dimerization and thereby channel opening (Zhang and Chen, 2016). In human CFTR, we also resolve an additional helical structure wedged into the intracellular space between the two halves of the molecule, interacting with TM helices 9, 10, and 12 (Figure 4A). Because the density of this region is positioned so as to connect to the elbow helix in TMD2 (Figure S3), it most likely corresponds to residues 825–843 of the R domain ($R_{825–843}$).

Although there is no phosphorylation site within residues 825–843, the overall charge of this region is very negative: it contains seven aspartate and glutamate residues, which account for 37% of its amino acid composition. Many polar residues in TMD2 are in van der Waals's contact with $R_{825–843}$ (Figure 4A). Among these potential interacting residues, substitutions of K978 with cysteine, serine, or proline were shown to increase CFTR channel activity independent of ATP (Wang et al., 2010). It would seem possible that removing the positive charge at position 978 lowers the affinity for $R_{825–843}$, thus facilitating R domain release from its inhibitory position.

To further illustrate the fact that $R_{825–843}$ must relocate to allow the channel to open, we compared the local structure of CFTR with that of Sav1866, a nucleotide-bound ABC exporter in the outward-facing conformation (Dawson and Locher, 2007). As shown in Figure 4B, the intracellular cavity between the two helical bundles narrows upon NBD dimerization. This narrowing would be incompatible with the helical $R_{825–843}$ inserted as observed in the closed CFTR channel structure.

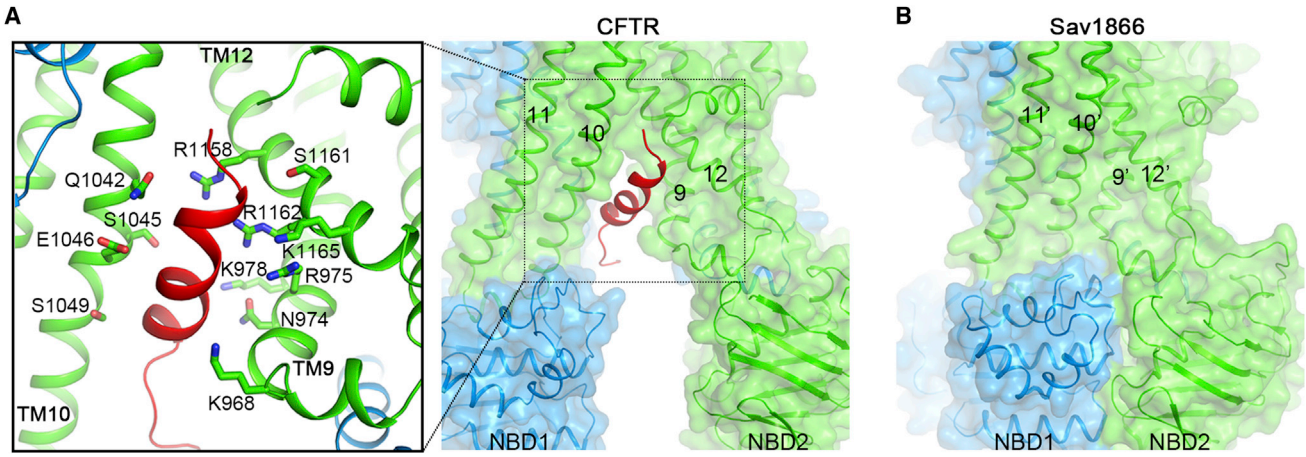


**Figure 4. The Dephosphorylated R Domain Inhibits Channel Opening**

(A) Residues 825–843 of the R domain (shown in red) insert into an opening between TM9 and TM10. Also shown in a close-up view are residues in van der Waals' contact with $R_{825–843}$, including K978.

(B) Structure of Sav1866 (PDB: 2ONJ) showing that helices corresponding to CFTR TM9 and TM10 are in close contact upon NBD dimerization.

See also Figure S3.

## Channel Activation by R Domain Phosphorylation

Easy access of PKA catalytic subunit (~30 kDa) to the R domain's multiple PKA consensus-site serines (Table S2) during channel activation by phosphorylation likely also requires the R domain to first be released from between the NBDs and TM extensions. Support for this comes from the sigmoid time course of current activation on sudden addition of a maximally activating concentration of PKA to membrane patches containing hundreds of human CFTR channels (Figure 5A). Fits of such current activations (in 11 patches) to a two-step process (e.g., like that in Figure 5B) yielded a slower (mean $k_{a1}$ = 0.07 ± 0.01 $s^{-1}$) and a faster (mean $k_{a2}$ = 0.26 ± 0.05 $s^{-1}$) rate for the two sequential activation steps. In contrast, application of a maximal PKA concentration to channels that are already partially activated increased current along an exponential time course, at a rate similar to that of the faster step, $k_{a2}$ (Csanády et al., 2005b). We therefore interpret the slower of the sequential steps to reflect infrequent spontaneous disengagement and release of the R domain and the faster step to reflect subsequent rapid phosphorylation of the R domain once released (strictly, because we are monitoring current, the faster rate $k_{a2}$ must also encompass the, even faster, channel opening step). Accordingly, the corresponding CFTR channel states are cartooned in Figure 5B as dephosphorylated ("D"), phosphorylatable ("P"), and maximally activated ("M"). The greatly magnified current segment inset in Figure 5A shows that individual channels occasionally, if rarely, open and close without having been phosphorylated by PKA; this current of unphosphorylated CFTR channels exposed to ATP was previously noted (Csanády et al., 2005a) to amount to 1.2% ± 0.5% (n = 13) of that after the same channels were maximally phosphorylated. Because even spontaneous opening of CFTR channels is accompanied by NBD dimerization (Mihályi et al., 2016), which in turn requires disengagement of the R domain, we propose that the rare openings of unphosphorylated channels in Figure 5A are enabled by comparably infrequent, reversible, R domain release events; those same rare releases of the R domain presumably also underlie the relatively weak ATPase activity of dephosphorylated CFTR (Figure 5E). This low ATPase rate and rare channel openings in the absence of PKA can be explained by the steady-state distribution of the CFTR population among D, P, and M states (Figure 5B) being shifted strongly leftward to only D and P states—with the slow D-to-P transition resulting in low fractional occupancy of state P, from which the rare ATP-driven gating and ATPase cycles can arise. In that case, most of the time, engaged R domains (state D) inhibit NBD dimerization, but occasional R domain release (to state P) supports a low level of activity. For occupancy of state P to remain low in the absence of PKA, spontaneous release of the R domain must be much slower than its spontaneous redocking. When PKA is present, relatively rapid phosphorylation of occasionally released R domains temporarily traps them, delaying their return to the inhibitory position and slowly accumulating the CFTR population in state M, hence accounting for the slow sigmoid time course of activation of channel current (Figures 5A and 5C). Dephosphorylation of the trapped R domains by phosphatases (transition M-to-P) allows them to spontaneously redock in the channel vestibule (transition P-to-D). These spontaneous motions of the R domain likely contribute to its evident disorder observed in the cryo-EM reconstruction (Figure 1).

## Correlation between CFTR Channel Gating Cycle and ATP Hydrolysis Rates

A record from a patch containing a single CFTR channel (Figure 5C) recapitulates the sequence of events observed for hundreds of channels (Figure 5A): the very low probability of seeing a CFTR channel open before phosphorylation, and the delay to the first opening after adding PKA, can both be attributed to infrequent disengagement of the unphosphorylated R domain (i.e., transition D-to-P; Figure 5B). Once phosphorylation of R domain serines reaches a steady state, so does channel gating.

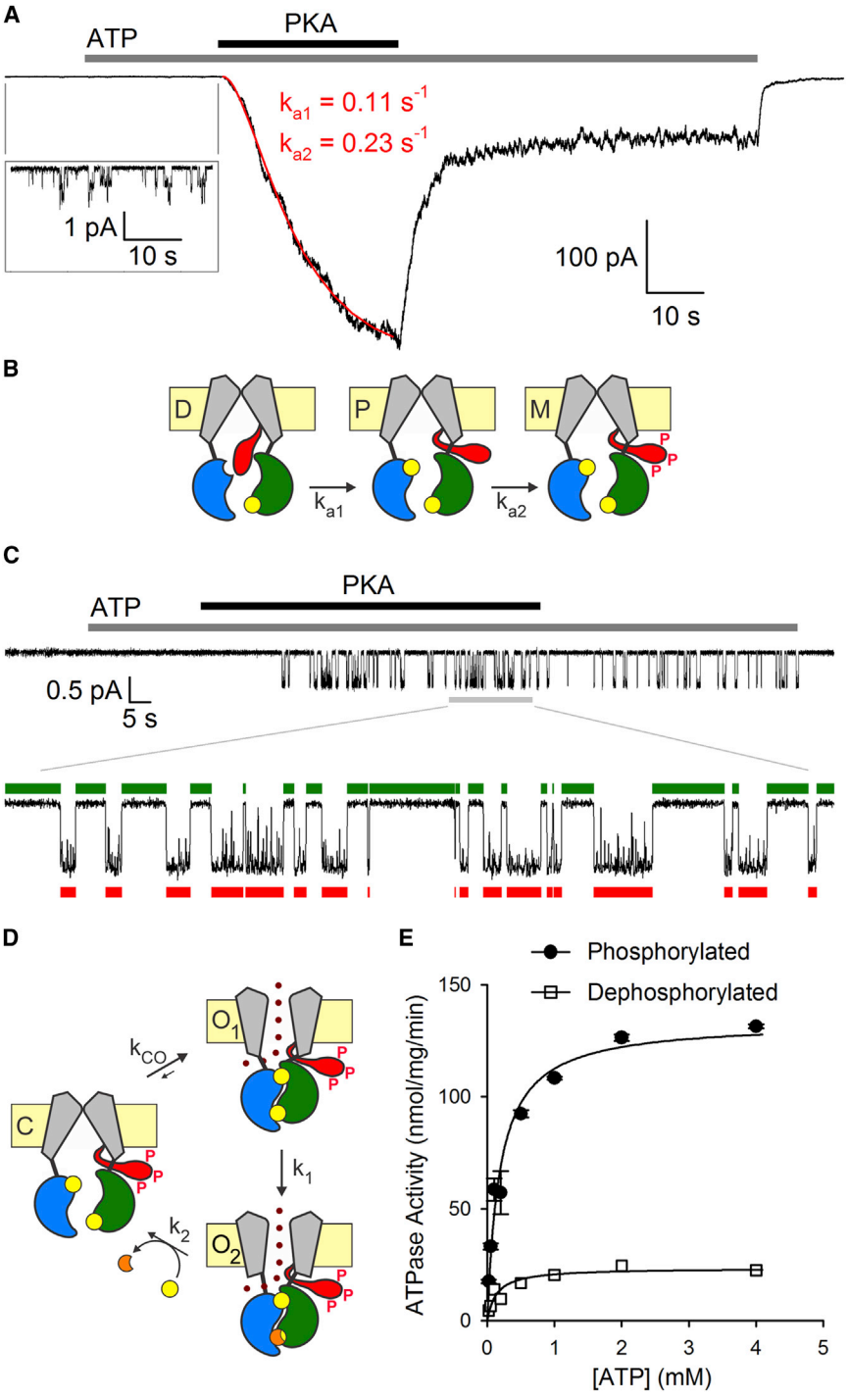


**Figure 5. PKA Phosphorylation Stimulates CFTR Channel Gating and ATPase Activity**

(A) Macroscopic current in an excised patch containing hundreds of human CFTR channels exposed to 2 mM MgATP shows only very few channel openings (amplified in inset at left) before phosphorylation, but is strongly stimulated along a sigmoid time course by 300 nM PKA catalytic subunit. The red line is a fit to the two-step activation scheme in (B) yielding the slower, $k_{a1}$, and faster, $k_{a2}$, rates indicated. PKA withdrawal allows endogenous phosphatases to partially dephosphorylate channels, diminishing the current in ATP.

(B) Cartoon model of two-step activation process of dephosphorylated ("D") channels. Infrequent, reversible, disengagement of the R domain (red tongue) from its inhibitory position slowly (with rate $k_{a1}$) renders channels phosphorylatable ("P"). Relatively rapid (rate $k_{a2}$) phosphorylation by PKA (indicated by red P on tongue) temporarily traps the R domain in a permissive position, rendering the channels maximally activated ("M") and allowing maximal channel gating via the cycle in (D). TMDs, gray; NBD1, blue; NBD2, green; R domain, red; ATP, yellow. Although steps D-to-P and P-to-M are both presumed reversible (the former spontaneously, the latter by phosphatase-mediated dephosphorylation), fitting the activation time course (in A) with the depicted two-parameter scheme estimates "net" rates of channel progression through the sequence of states D-P-M.

(C) Single-channel current recording with addition of 2 mM MgATP and 300 nM PKA as indicated. The thin gray bar beneath the record indicates the segment near the end of the exposure to PKA, magnified below, with green bars marking times, $\tau_{ib}$, the channel spent in the interburst closed state ("C" in D), and red bars marking times, $\tau_b$, spent in open burst states ("$O_1$" and "$O_2$" in D).

(D) Cartoon representation of gating cycle of fully phosphorylated CFTR channel. ATP-bound closed channels (state C) open, with rate $k_{CO} = 1/\tau_{ib}$, to a prehydrolytic open state ($O_1$), permitting flow of chloride ions (purple dots). ATP is split to ADP (orange) and $P_i$ at competent catalytic site 2 (rate $k_1$), leading to dimer disruption (rate $k_2$) that causes channel closure. The open burst duration, $\tau_b$, comprises time spent sequentially in both $O_1$ and $O_2$ states.

(E) ATPase rate at 28°C of purified human CFTR as a function of ATP concentration after PKA phosphorylation (filled circles) or after dephosphorylation with lambda phosphatase (empty squares). The curves show Michaelis-Menten fits, yielding for phosphorylated CFTR, Km = 187 ± 24 μM, $V_{max}$ = 134 ± 4 nmol/mg/min and for dephosphorylated CFTR, Km = 138 ± 30 μM, $V_{max}$ = 23 ± 1 nmol/mg/min.

See also Figure S4 and Table S2.

In the latter cyclic process, two ATPs are bound in the closed-channel state, C (Figure 5D; equivalent to state M in Figure 5B) then sandwiched at the NBD dimer interface, so signaling the channel gate to open (state $O_1$) until the ATP at the competent, consensus, site is hydrolyzed (state $O_2$), which leads to dimer disruption, nucleotide exchange, and channel closure (state C).

A 20-s segment of the record (gray bar, Figure 5C) is shown magnified, with individual closed periods and open bursts marked. Each green bar measures time the channel spent in closed state C (interburst duration, $\tau_{ib}$), and each red bar measures time spent in an open burst, in state $O_1$ and then $O_2$ (open burst duration, $\tau_b$). Because >95% of all human

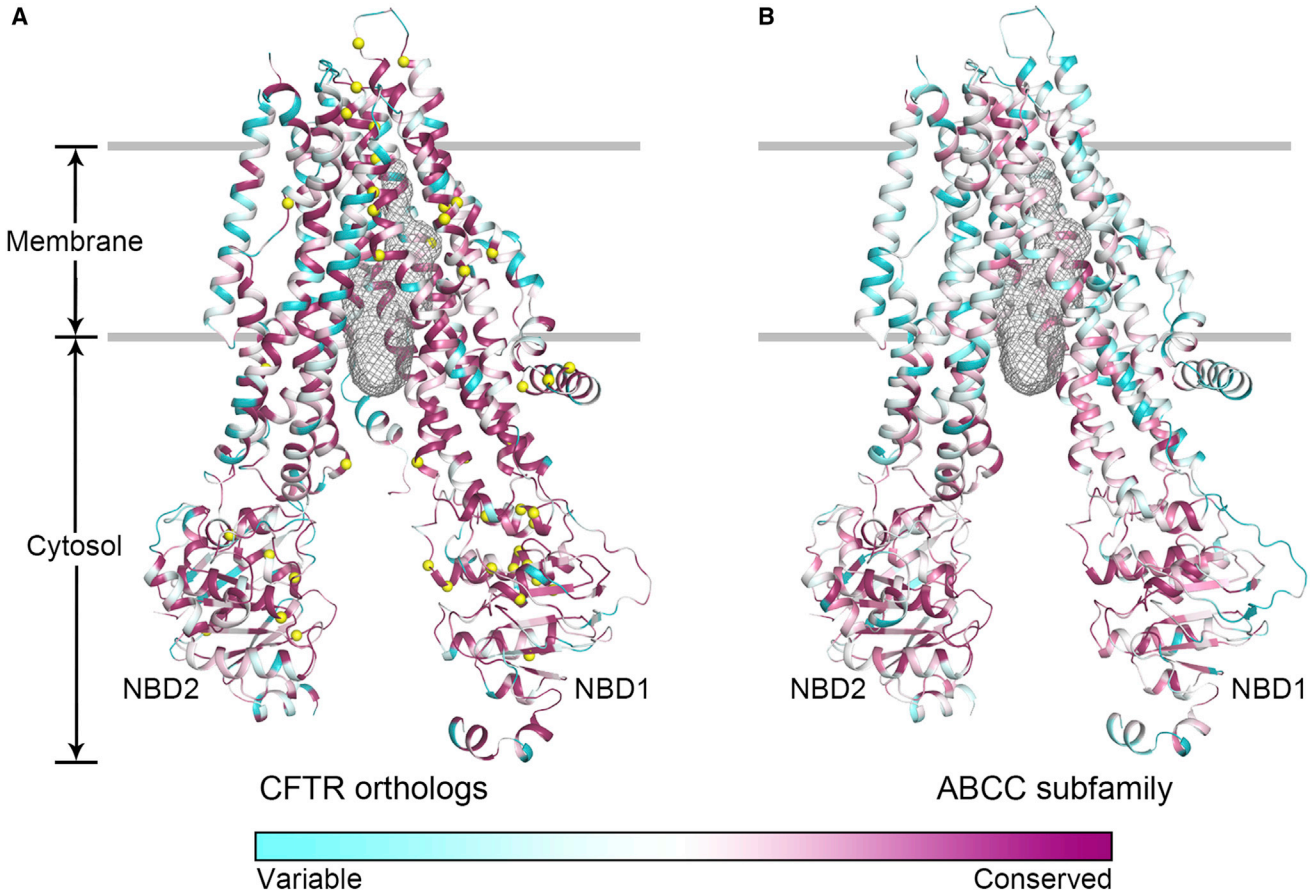


**Figure 6. Sequence Conservation Analysis**

(A) Sequence conservation analysis of 11 CFTR orthologs. The pairwise sequence identity of human CFTR and its orthologs are: human (100%), pig (92%), rabbit (92%), ferret (92%), sheep (91%), chicken (80%), mouse (78%), *Xenopus* (77%), shark (71%), killifish (58%), and zebrafish (55%). The locations of the 53 missense cystic fibrosis-causing mutations are indicated by yellow spheres.

(B) Sequence conservation of the 12 human ABCC proteins mapped onto the structure of CFTR. The $R_{825–843}$ segment is omitted as it is only found in CFTR.

CFTR channel openings are terminated by hydrolysis of a single ATP (Csanády et al., 2010), on average the time for completion of the gating cycle, i.e., $\tau_{ib} + \tau_b$, which was 1.91 ± 0.5 s for nine fully phosphorylated CFTR channels (including the one in Figure 5C) must be identical to that for completion of the ATPase cycle. In other words, the mean gating cycle rate, $1/(\tau_{ib} + \tau_b)$, ~0.52 $s^{-1}$ for these channels in saturating ATP, at 25°C, should match the maximal ATPase turnover rate determined under comparable conditions. ATPase rates of dephosphorylated and fully phosphorylated (Figure S4) purified human CFTR over a range of ATP concentrations at 28°C reveal strong activation (~6-fold) by PKA (Figure 5E), as similarly observed for purified zebrafish CFTR (Zhang and Chen, 2016). The maximum ATPase rate of phosphorylated human CFTR, 134 nmol/mg/min (Figure 5E), corresponds to a maximal cycle turnover rate of 0.37 $s^{-1}$, assuming that 100% of the purified protein is active in detergent. Given the variability of estimates of human CFTR channel gating cycle rates in 300–550 nM PKA, 2–5 mM ATP, at 21°C–26°C (0.47 $s^{-1}$ [Csanády et al., 2000], 0.45 $s^{-1}$ [Vergani et al., 2003], 0.53 $s^{-1}$ [Csanády et al., 2005a], 0.72 $s^{-1}$ [Csanády et al., 2005b], 0.62 $s^{-1}$ [Csanády et al., 2010]), we can conclude that up to 84% of the purified human protein retains full activity.

## CFTR Compared to Other ABCC Transporters

The ABC transporter family includes thousands of proteins found in all living species, out of which only CFTR is known to function as an ion channel. Almost all other ABC transporters are active pumps that translocate substrates against their electrochemical gradients (Theodoulou and Kerr, 2015). We ask if there are any special structural features that render CFTR a channel instead of a pump.

First, we analyzed sequence conservation among 11 functionally characterized CFTR orthologs (Aleksandrov et al., 2012; Cai et al., 2015; Clarke et al., 1992; Kopelman et al., 1995; Marshall et al., 1991; Price et al., 1996; Riordan et al., 1989; Rogers et al., 2008; Singer et al., 1998; Sun et al., 2010; Zhang and Chen, 2016). The pairwise sequence identity between human CFTR and each ortholog used in this analysis varies from 55% (zebrafish) to 92% (pig). Highly conserved residues are found throughout the pore, the cytosolic extensions of the TM helices, and the NBDs (Figure 6A). The degree of sequence conservation

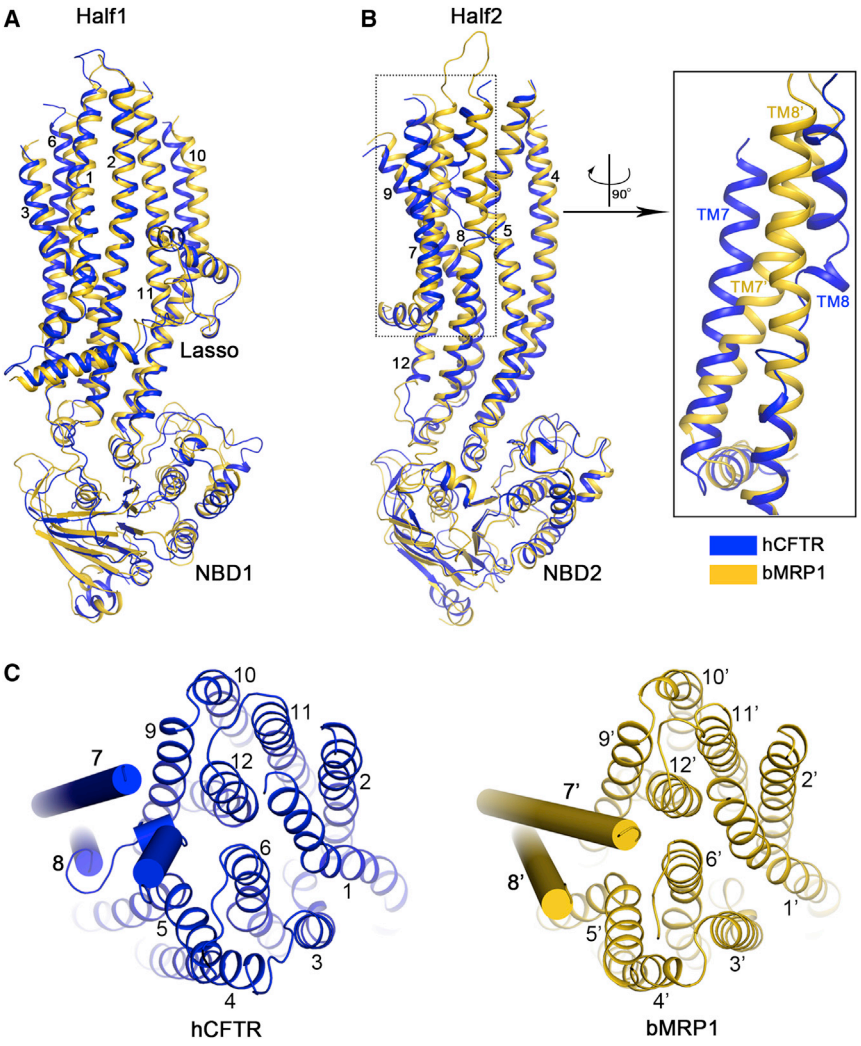


**Figure 7. Structural Comparison of CFTR and MRP1**

Human CFTR (hCFTR) is shown in blue and bovine MRP1 (bMRP1, PDB: 5UJA) in yellow. Because bMRP1 contains an additional TMD0 domain (not shown), helices are numbered based on the CFTR structure.

(A) Superimposition of half1, which comprises the lasso motif, 6 TM helices, and NBD1.

(B) Superimposition of the other half. Also shown is a zoom-in view of TM7 and TM8.

(C) The 12 TM helices viewed from the extracellular side of the membrane. TM7 and TM8 are shown in cylinder and other helices in ribbon.

correlates well with the mutations that cause cystic fibrosis (https://cftr2.org). Thus, the majority of the 53 missense mutations (Figure 6A, yellow spheres) occur within highly conserved positions, underscoring the importance of these regions in maintaining the structural and functional integrity of CFTR.

Next, we extended this analysis to the ABCC subfamily, which includes members that are closely related in sequence but diverse in function. In addition to CFTR, the ABCC subfamily includes nine multidrug-resistance proteins (MRP1-9) that are ATP-driven efflux pumps and two sulfonylurea receptors (SUR1 and SUR2) with no known transport substrates (Vasiliou et al., 2009). The SUR proteins regulate the activity of potassium channels in the context of complexes known as $K_{ATP}$ channels (Inagaki et al., 1996; Martin et al., 2017). When mapped onto the structure of CFTR, conserved residues in this subfamily are mainly found in the cytosolic region of the protein, such as the NBD catalytic cores, the surfaces of the intracellular vestibule, and the NBD/TMD interfaces (Figure 6B). Sequences in the TM region are highly variable, consistent with the distinct functions of CFTR, MRP, and SUR. These results also suggest that ATP binding to the different ABCC proteins would induce a similar dimerization of the NBDs and coming together of the intracellular extensions of the TMDs to create interactions like those depicted in Figure 4B.

To understand the structural differences between a channel and pump in the same ABCC subfamily, we directly compared the structures of CFTR and MRP1 (Johnson and Chen, 2017) (PDB: 5UJA). One half of CFTR, comprising the lasso motif, TM helices 1, 2, 3, 6, 10, 11, and NBD1, superimposes very well with the corresponding regions of MRP1 (Figure 7A). The structure of the other half of CFTR is also similar to that of MRP1, except for TM helices 7 and 8 (Figure 7B). In MRP1 both TM7 and TM8 are continuous helices, typical of other ABC transporters. In CFTR, however, TM8 breaks into three short helices and TM7 is displaced from its usual position (Figures 7B and 7C). A mutation within the helical break, L927P, causes cystic fibrosis, possibly by altering the flexibility of TM8. Helical breaks inside the low dielectric core of the membrane can create potential ion binding sites (Doyle et al., 1998; Dutzler et al., 2002) and flexible hinges to facilitate gating. As TM8 lines the pore, it could play a critical role in ion conduction and gating. This unique feature of CFTR is likely the structural basis for its channel function.

In summary, we presented here the cryo-EM structure of human CFTR determined in the dephosphorylated, ATP-free conformation. The structure was analyzed to further establish the architecture of the ion pore, the functions of many positively charged residues, and to identify the structural basis for CFTR's channel activity. We showed how the observed location of the R domain informs understanding of CFTR's slow activation by phosphorylation, as well as of infrequent cycling by unphosphorylated CFTR. We also analyzed the relationship between ATP hydrolysis and channel gating, illuminating how these two events correlate in a CFTR duty cycle.

## STAR★METHODS

Detailed methods are provided in the online version of this paper and include the following:

- KEY RESOURCES TABLE
- CONTACT FOR REAGENT AND RESOURCE SHARING
- EXPERIMENTAL MODEL AND SUBJECT DETAILS
  - Cell Culture
  - Isolation and injection of *Xenopus laevis* oocytes
- METHOD DETAILS
  - Expression and Purification of Protein
  - ATPase Activity Assay
  - Electrophysiology
  - EM Sample Preparation and Data collection
  - Imaging Processing and 3D reconstruction
  - Model Construction
  - Model Refinement and Validation
  - Sequence conservation analysis
- QUANTIFICATION AND STATISTICAL ANALYSIS
- DATA AND SOFTWARE AVAILABILITY

### SUPPLEMENTAL INFORMATION

Supplemental Information includes four figures and two tables and can be found with this article online at http://dx.doi.org/10.1016/j.cell.2017.02.024.

### AUTHOR CONTRIBUTIONS

F.L. expressed and purified human CFTR protein and measured the ATPase activities presented in Figure 5E. Z.Z. and F.L. collected and processed cryo-EM data. Z.Z. built and refined the model. L.C. performed channel recordings and analysis presented in Figure 5. D.C.G. and J.C. wrote the manuscript with inputs from all authors.

### ACKNOWLEDGMENTS

We thank Eric Gouaux for the expression vector, Mark Ebrahim and Johanna Sotiris at the Rockefeller Evelyn Gruss Lipper Cryo-Electron Microscopy Resource Center for assistance in data collection, and Sarah McCarry for editing this manuscript. This work is supported by the Rockefeller University (to J.C. and D.C.G), the Howard Hughes Medical Institute (to J.C.), and MTA-Momentum (LP2012-39/2012) and Cystic Fibrosis Foundation (CSANAD15G0) grants (to L.C.).

Received: January 27, 2017
Revised: February 9, 2017
Accepted: February 14, 2017
Published: March 23, 2017

### SUPPORTING CITATIONS

The following references appear in the Supplemental Information: Gadsby and Nairn (1999); Sebastian et al. (2013); Wilkinson et al (1997).

### REFERENCES

Adams, P.D., Afonine, P.V., Bunkóczi, G., Chen, V.B., Davis, I.W., Echols, N., Headd, J.J., Hung, L.W., Kapral, G.J., Grosse-Kunstleve, R.W., et al. (2010). PHENIX: a comprehensive Python-based system for macromolecular structure solution. Acta Crystallogr. D Biol. Crystallogr. *66*, 213–221.

Aleksandrov, A.A., Kota, P., Cui, L., Jensen, T., Alekseev, A.E., Reyes, S., He, L., Gentzsch, M., Aleksandrov, L.A., Dokholyan, N.V., and Riordan, J.R. (2012). Allosteric modulation balances thermodynamic stability and restores function of ΔF508 CFTR. J. Mol. Biol. *419*, 41–60.

Ashkenazy, H., Abadi, S., Martz, E., Chay, O., Mayrose, I., Pupko, T., and Ben-Tal, N. (2016). ConSurf 2016: an improved methodology to estimate and visualize evolutionary conservation in macromolecules. Nucleic Acids Res. *44*(W1), W344-50.

Aubin, C.N., and Linsdell, P. (2006). Positive charges at the intracellular mouth of the pore regulate anion conduction in the CFTR chloride channel. J. Gen. Physiol. *128*, 535–545.

Boat, T.F., Welsh, M.J., and Beaudet, A.L. (1989). The Metabolic Basis of Inherited Disease, Sixth Edition, C.R. Scriver, A.L. Beaudet, W.S. Sly, and D. Valle, eds. (McGraw-Hill), pp. 2649–2680.

Brown, A., Long, F., Nicholls, R.A., Toots, J., Emsley, P., and Murshudov, G. (2015). Tools for macromolecular model building and refinement into electron cryo-microscopy reconstructions. Acta Crystallogr. D Biol. Crystallogr. *71*, 136–153.

Cai, Z., Palmai-Pallag, T., Khuituan, P., Mutolo, M.J., Boinot, C., Liu, B., Scott-Ward, T.S., Callebaut, I., Harris, A., and Sheppard, D.N. (2015). Impact of the F508del mutation on ovine CFTR, a Cl- channel with enhanced conductance and ATP-dependent gating. J. Physiol. *593*, 2427–2446.

Chen, V.B., Arendall, W.B., 3rd, Headd, J.J., Keedy, D.A., Immormino, R.M., Kapral, G.J., Murray, L.W., Richardson, J.S., and Richardson, D.C. (2010). MolProbity: all-atom structure validation for macromolecular crystallography. Acta Crystallogr. D Biol. Crystallogr. *66*, 12–21.

Cheng, S.H., Rich, D.P., Marshall, J., Gregory, R.J., Welsh, M.J., and Smith, A.E. (1991). Phosphorylation of the R domain by cAMP-dependent protein kinase regulates the CFTR chloride channel. Cell *66*, 1027–1036.

Clarke, L.L., Grubb, B.R., Gabriel, S.E., Smithies, O., Koller, B.H., and Boucher, R.C. (1992). Defective epithelial chloride transport in a gene-targeted mouse model of cystic fibrosis. Science *257*, 1125–1128.

Csanády, L. (2000). Rapid kinetic analysis of multichannel records by a simultaneous fit to all dwell-time histograms. Biophys. J. *78*, 785–799.

Csanády, L., Chan, K.W., Seto-Young, D., Kopsco, D.C., Nairn, A.C., and Gadsby, D.C. (2000). Severed channels probe regulation of gating of cystic fibrosis transmembrane conductance regulator by its cytoplasmic domains. J. Gen. Physiol. *116*, 477–500.

Csanády, L., Chan, K.W., Nairn, A.C., and Gadsby, D.C. (2005a). Functional roles of nonconserved structural segments in CFTR's NH2-terminal nucleotide binding domain. J. Gen. Physiol. *125*, 43–55.

Csanády, L., Seto-Young, D., Chan, K.W., Cenciarelli, C., Angel, B.B., Qin, J., McLachlin, D.T., Krutchinsky, A.N., Chait, B.T., Nairn, A.C., and Gadsby, D.C. (2005b). Preferential phosphorylation of R-domain Serine 768 dampens activation of CFTR channels by PKA. J. Gen. Physiol. *125*, 171–186.

Csanády, L., Vergani, P., and Gadsby, D.C. (2010). Strict coupling between CFTR's catalytic cycle and gating of its Cl- ion pore revealed by distributions of open channel burst durations. Proc. Natl. Acad. Sci. USA *107*, 1241–1246.

Davis, I.W., Leaver-Fay, A., Chen, V.B., Block, J.N., Kapral, G.J., Wang, X., Murray, L.W., Arendall, W.B., 3rd, Snoeyink, J., Richardson, J.S., and Richardson, D.C. (2007). MolProbity: all-atom contacts and structure validation for proteins and nucleic acids. Nucleic Acids Res. *35*, W375-83.

Dawson, R.J., and Locher, K.P. (2007). Structure of the multidrug ABC transporter Sav1866 from Staphylococcus aureus in complex with AMP-PNP. FEBS Lett. *581*, 935–938.

Doyle, D.A., Morais Cabral, J., Pfuetzner, R.A., Kuo, A., Gulbis, J.M., Cohen, S.L., Chait, B.T., and MacKinnon, R. (1998). The structure of the potassium channel: molecular basis of K+ conduction and selectivity. Science *280*, 69–77.

Dutzler, R., Campbell, E.B., Cadene, M., Chait, B.T., and MacKinnon, R. (2002). X-ray structure of a ClC chloride channel at 3.0 A reveals the molecular basis of anion selectivity. Nature *415*, 287–294.

El Hiani, Y., and Linsdell, P. (2015). Functional architecture of the cytoplasmic entrance to the cystic fibrosis transmembrane conductance regulator chloride channel pore. J. Biol. Chem. *290*, 15855–15865.

Emsley, P., Lohkamp, B., Scott, W.G., and Cowtan, K. (2010). Features and development of Coot. Acta Crystallogr. D Biol. Crystallogr. *66*, 486–501.

Frank, G.A., Shukla, S., Rao, P., Borgnia, M.J., Bartesaghi, A., Merk, A., Mobin, A., Esser, L., Earl, L.A., Gottesman, M.M., et al. (2016). Cryo-EM analysis of the conformational landscape of human P-glycoprotein (ABCB1) during its catalytic cycle. Mol. Pharmacol. *90*, 35–41.

Gadsby, D.C., and Nairn, A.C. (1999). Control of CFTR channel gating by phosphorylation and nucleotide hydrolysis. Physiol. Rev. *79*(1, Suppl), S77–S107.

Gadsby, D.C., Vergani, P., and Csanády, L. (2006). The ABC protein turned chloride channel whose failure causes cystic fibrosis. Nature *440*, 477–483.

Ge, N., Muise, C.N., Gong, X., and Linsdell, P. (2004). Direct comparison of the functional roles played by different transmembrane regions in the cystic fibrosis transmembrane conductance regulator chloride channel pore. J. Biol. Chem. *279*, 55283–55289.

Goehring, A., Lee, C.H., Wang, K.H., Michel, J.C., Claxton, D.P., Baconguis, I., Althoff, T., Fischer, S., Garcia, K.C., and Gouaux, E. (2014). Screening and large-scale expression of membrane proteins in mammalian cells for structural studies. Nat. Protoc. *9*, 2574–2585.

Gong, X., and Linsdell, P. (2003). Mutation-induced blocker permeability and multiion block of the CFTR chloride channel pore. J. Gen. Physiol. *122*, 673–687.

Grant, T., and Grigorieff, N. (2015). Measuring the optimal exposure for single particle cryo-EM using a 2.6 Å reconstruction of rotavirus VP6. eLife *4*, e06980.

Grigorieff, N. (2016). Frealign: an exploratory tool for single-particle cryo-EM. Methods Enzymol. *579*, 191–226.

Gunderson, K.L., and Kopito, R.R. (1995). Conformational states of CFTR associated with channel gating: the role ATP binding and hydrolysis. Cell *82*, 231–239.

Heijne, G. (1986). The distribution of positively charged residues in bacterial inner membrane proteins correlates with the trans-membrane topology. EMBO J. *5*, 3021–3027.

Heymann, J.B., and Belnap, D.M. (2007). Bsoft: image processing and molecular modeling for electron microscopy. J. Struct. Biol. *157*, 3–18.

Inagaki, N., Gonoi, T., Clement, J.P., Wang, C.Z., Aguilar-Bryan, L., Bryan, J., and Seino, S. (1996). A family of sulfonylurea receptors determines the pharmacological properties of ATP-sensitive K+ channels. Neuron *16*, 1011–1017.

Johnson, Z.L., and Chen, J. (2017). Structural Basis of Substrate Recognition by the Multidrug Resistance Protein MRP1. Cell *168*, 1075–1085 e1079.

Kelley, L.A., Mezulis, S., Yates, C.M., Wass, M.N., and Sternberg, M.J. (2015). The Phyre2 web portal for protein modeling, prediction and analysis. Nat. Protoc. *10*, 845–858.

Kopelman, H., Ferretti, E., Gauthier, C., and Goodyer, P.R. (1995). Rabbit pancreatic acini express CFTR as a cAMP-activated chloride efflux pathway. Am. J. Physiol. *269*, C626–C631.

Larkin, M.A., Blackshields, G., Brown, N.P., Chenna, R., McGettigan, P.A., McWilliam, H., Valentin, F., Wallace, I.M., Wilm, A., Lopez, R., et al. (2007). Clustal W and Clustal X version 2.0. Bioinformatics *23*, 2947–2948.

Linsdell, P. (2017). Architecture and functional properties of the CFTR channel pore. Cell. Mol. Life Sci. *74*, 67–83.

Magleby, K.L., and Pallotta, B.S. (1983). Burst kinetics of single calcium-activated potassium channels in cultured rat muscle. J. Physiol. *344*, 605–623.

Marshall, J., Martin, K.A., Picciotto, M., Hockfield, S., Nairn, A.C., and Kaczmarek, L.K. (1991). Identification and localization of a dogfish homolog of human cystic fibrosis transmembrane conductance regulator. J. Biol. Chem. *266*, 22749–22754.

Martin, G.M., Yoshioka, C., Rex, E.A., Fay, J.F., Xie, Q., Whorton, M.R., Chen, J.Z., and Shyng, S.L. (2017). Cryo-EM structure of the ATP-sensitive potassium channel illuminates mechanisms of assembly and gating. eLife *6*, e24149.

Mastronarde, D.N. (2005). Automated electron microscope tomography using robust prediction of specimen movements. J. Struct. Biol. *152*, 36–51.

Mihályi, C., Töröcsik, B., and Csanády, L. (2016). Obligate coupling of CFTR pore opening to tight nucleotide-binding domain dimerization. eLife *5*, e18164.

Moeller, A., Lee, S.C., Tao, H., Speir, J.A., Chang, G., Urbatsch, I.L., Potter, C.S., Carragher, B., and Zhang, Q. (2015). Distinct conformational spectrum of homologous multidrug ABC transporters. Structure *23*, 450–460.

Murshudov, G.N., Vagin, A.A., and Dodson, E.J. (1997). Refinement of macromolecular structures by the maximum-likelihood method. Acta Crystallogr. D Biol. Crystallogr. *53*, 240–255.

Nilsson, J., Persson, B., and von Heijne, G. (2005). Comparative analysis of amino acid distributions in integral membrane proteins from 107 genomes. Proteins *60*, 606–616.

Pettersen, E.F., Goddard, T.D., Huang, C.C., Couch, G.S., Greenblatt, D.M., Meng, E.C., and Ferrin, T.E. (2004). UCSF Chimera–a visualization system for exploratory research and analysis. J. Comput. Chem. *25*, 1605–1612.

Price, M.P., Ishihara, H., Sheppard, D.N., and Welsh, M.J. (1996). Function of Xenopus cystic fibrosis transmembrane conductance regulator (CFTR) Cl channels and use of human-Xenopus chimeras to investigate the pore properties of CFTR. J. Biol. Chem. *271*, 25184–25191.

Riordan, J.R., Rommens, J.M., Kerem, B., Alon, N., Rozmahel, R., Grzelczak, Z., Zielenski, J., Lok, S., Plavsic, N., Chou, J.L., et al. (1989). Identification of the cystic fibrosis gene: cloning and characterization of complementary DNA. Science *245*, 1066–1073.

Rogers, C.S., Stoltz, D.A., Meyerholz, D.K., Ostedgaard, L.S., Rokhlina, T., Taft, P.J., Rogan, M.P., Pezzulo, A.A., Karp, P.H., Itani, O.A., et al. (2008). Disruption of the CFTR gene produces a model of cystic fibrosis in newborn pigs. Science *321*, 1837–1841.

Rohou, A., and Grigorieff, N. (2015). CTFFIND4: Fast and accurate defocus estimation from electron micrographs. J. Struct. Biol. *192*, 216–221.

Rommens, J.M., Iannuzzi, M.C., Kerem, B., Drumm, M.L., Melmer, G., Dean, M., Rozmahel, R., Cole, J.L., Kennedy, D., Hidaka, N., et al. (1989). Identification of the cystic fibrosis gene: chromosome walking and jumping. Science *245*, 1059–1065.

Rubinstein, J.L., and Brubaker, M.A. (2015). Alignment of cryo-EM movies of individual particles by optimization of image translations. J. Struct. Biol. *192*, 188–195.

Scharschmidt, B.F., Keeffe, E.B., Blankenship, N.M., and Ockner, R.K. (1979). Validation of a recording spectrophotometric method for measurement of membrane-associated Mg- and NaK-ATPase activity. J. Lab. Clin. Med. *93*, 790–799.

Scheres, S.H. (2012). RELION: implementation of a Bayesian approach to cryo-EM structure determination. J. Struct. Biol. *180*, 519–530.

Scheres, S.H., and Chen, S. (2012). Prevention of overfitting in cryo-EM structure determination. Nat. Methods *9*, 853–854.

Sebastian, A., Rishishwar, L., Wang, J., Bernard, K.F., Conley, A.B., McCarty, N.A., and Jordan, I.K. (2013). Origin and evolution of the cystic fibrosis transmembrane regulator protein R domain. Gene *523*, 137–146.

Singer, T.D., Tucker, S.J., Marshall, W.S., and Higgins, C.F. (1998). A divergent CFTR homologue: highly regulated salt transport in the euryhaline teleost F. heteroclitus. Am. J. Physiol. *274*, C715–C723.

Smart, O.S., Neduvelil, J.G., Wang, X., Wallace, B.A., and Sansom, M.S. (1996). HOLE: a program for the analysis of the pore dimensions of ion channel structural models. J. Mol. Graph. *14*, 354–360, 376.

Smith, S.S., Liu, X., Zhang, Z.R., Sun, F., Kriewall, T.E., McCarty, N.A., and Dawson, D.C. (2001). CFTR: covalent and noncovalent modification suggests a role for fixed charges in anion conduction. J. Gen. Physiol. *118*, 407–431.

Sun, X., Sui, H., Fisher, J.T., Yan, Z., Liu, X., Cho, H.J., Joo, N.S., Zhang, Y., Zhou, W., Yi, Y., et al. (2010). Disease phenotype of a ferret CFTR-knockout model of cystic fibrosis. J. Clin. Invest. *120*, 3149–3160.

Ten Eyck, L.F. (1977). Efficient structure-factor calculation for large molecules by the fast fourier transform. Acta Crystallogr. A *33*, 486–492.

Theodoulou, F.L., and Kerr, I.D. (2015). ABC transporter research: going strong 40 years on. Biochem. Soc. Trans. *43*, 1033–1040.

Vasiliou, V., Vasiliou, K., and Nebert, D.W. (2009). Human ATP-binding cassette (ABC) transporter family. Hum. Genomics *3*, 281–290.

Vergani, P., Nairn, A.C., and Gadsby, D.C. (2003). On the mechanism of MgATP-dependent gating of CFTR Cl- channels. J. Gen. Physiol. *121*, 17–36.

Vergani, P., Lockless, S.W., Nairn, A.C., and Gadsby, D.C. (2005). CFTR channel opening by ATP-driven tight dimerization of its nucleotide-binding domains. Nature *433*, 876–880.

Wang, W., Wu, J., Bernard, K., Li, G., Wang, G., Bevensee, M.O., and Kirk, K.L. (2010). ATP-independent CFTR channel gating and allosteric modulation by phosphorylation. Proc. Natl. Acad. Sci. USA *107*, 3888–3893.

Wang, Z., Hryc, C.F., Bammes, B., Afonine, P.V., Jakana, J., Chen, D.H., Liu, X., Baker, M.L., Kao, C., Ludtke, S.J., et al. (2014). An atomic model of brome mosaic virus using direct electron detection and real-space optimization. Nat. Commun. *5*, 4808.

Ward, A.B., Szewczyk, P., Grimard, V., Lee, C.W., Martinez, L., Doshi, R., Caya, A., Villaluz, M., Pardon, E., Cregger, C., et al. (2013). Structures of P-glycoprotein reveal its conformational flexibility and an epitope on the nucleotide-binding domain. Proc. Natl. Acad. Sci. USA *110*, 13386–13391.

Webb, B., and Sali, A. (2014). Comparative protein structure modeling using MODELLER. Curr. Protoc. Bioinformatics *47*, 5.6.1-32.

Wilkinson, D.J., Strong, T.V., Mansoura, M.K., Wood, D.L., Smith, S.S., Collins, F.S., and Dawson, D.C. (1997). CFTR activation: additive effects of stimulatory and inhibitory phosphorylation sites in the R domain. Am. J. Physiol. *273*, L127–L133.

Zhang, Z., and Chen, J. (2016). Atomic structure of the cystic fibrosis transmembrane conductance regulator. Cell *167*, 1586–1597.

Zhang, J., and Hwang, T.C. (2015). The fifth transmembrane segment of cystic fibrosis transmembrane conductance regulator contributes to its anion permeation pathway. Biochemistry *54*, 3839–3850.

Zhou, J.J., Fatehi, M., and Linsdell, P. (2007). Direct and indirect effects of mutations at the outer mouth of the cystic fibrosis transmembrane conductance regulator chloride channel pore. J. Membr. Biol. *216*, 129–142.

Zhou, J.J., Fatehi, M., and Linsdell, P. (2008). Identification of positive charges situated at the outer mouth of the CFTR chloride channel pore. Pflugers Arch. *457*, 351–360.

Zhou, J.J., Li, M.S., Qi, J., and Linsdell, P. (2010). Regulation of conductance by the number of fixed positive charges in the intracellular vestibule of the CFTR chloride channel pore. J. Gen. Physiol. *135*, 229–245.

## STAR★METHODS

### KEY RESOURCES TABLE

| REAGENT or RESOURCE | SOURCE | IDENTIFIER |
|---|---|---|
| Chemicals, Peptides, and Recombinant Proteins | | |
| 2,2-didecylpropane-1,3-bis-β-D-maltopyranoside (LMNG) | Anatrace | NG310 |
| Cholesteryl hemisuccinate (CHS) | Anatrace | CH210 |
| Digitonin | Sigma-Aldrich | D141 |
| sf-900 II SFM medium | GIBCO | Cat#10902-088 |
| Cellfectin II reagents | Invitrogen | Cat#10362-100 |
| Freestyle 293 medium | GIBCO | Cat#12338-018 |
| Lambda PP | NEB | Cat#P0753L |
| PKA catalytic subunit, recombinant | NEB | Cat#P6000L |
| PKA catalytic subunit, bovine | Sigma-Aldrich | P2645 |
| ATP | Sigma-Aldrich | A2383 |
| MgATP | Sigma-Aldrich | A9187 |
| Pyruvate kinase | Roche | 10128163001 |
| Lactate dehydrogenase | Roche | 10127876001 |
| Phosphoenolpyruvate | Roche | 10108294001 |
| NADH | Roche | 10107735001 |
| mMessage T7 transcription kit | ThermoFisher | Cat#AM1344 |
| Critical Commercial Assays | | |
| CNBR-activated Sepharose beads | GE Healthcare | 17-0430-01 |
| Superose 6, 10/300 GL | GE Healthcare | 17-5172-01 |
| Deposited Data | | |
| Coordinates of the human CFTR | This paper | PDB: 5UAK |
| Cryo-EM map of the human CFTR | This paper | EMDB: EMD-8516 |
| Coordinates of zebrafish CFTR | Zhang and Chen, 2016 | PDB: 5UAR |
| Coordinates of Sav1866 | Dawson and Locher, 2007 | PDB: 2ONJ |
| Coordinates of MRP1 | Johnson and Chen, 2017 | PDB: 5UJA |
| Experimental Models: Cell Lines | | |
| Sf9 | ATCC | CRL-1711 |
| HEK293S GnTI$^{-}$ | ATCC | CRL-3022 |
| Recombinant DNA | | |
| Codon-optimized human CFTR in pUC57 vector | BioBasic | N/A |
| Human CFTR cloned onto a modified pEG Bacmam vector suitable for expression in mammalian cells | This paper | N/A |
| Human CFTR cloned into pGEMHE vector for in vitro transcription | This paper | N/A |
| Sequence-Based Reagents | | |
| Primer: Forward: CCGCTCGAGCCA CCATGCAGCGTTCACCTCTGGAAAAA | IDT | N/A |
| Primer: Reverse: CCGGAATTCGAAAG TCTGGTATCCTGGACTTCCTCC | IDT | N/A |
| Software and Algorithms | | |
| Seriel EM | Mastronarde, 2005 | http://bio3d.colorado.edu/SerialEM |

(*Continued on next page*)

*Continued*

| REAGENT or RESOURCE | SOURCE | IDENTIFIER |
|---|---|---|
| Unblur | Grant and Grigorieff, 2015 | http://grigoriefflab.janelia.org/unblur |
| CTFFIND4 | Rohou and Grigorieff, 2015 | http://grigoriefflab.janelia.org/ctffind4 |
| RELION 1.4 | Scheres, 2012 | http://www2.mrc-lmb.cam.ac.uk/relion |
| alignparts_lmbfgs | Rubinstein and Brubaker, 2015 | https://sites.google.com/site/rubinsteingroup/direct-detector-align_lmbfgs |
| FREALIGN | Grigorieff, 2016 | http://grigoriefflab.janelia.org/frealign |
| COOT | Emsley et al., 2010 | https://www2.mrc-lmb.cam.ac.uk/personal/pemsley/coot |
| Modeler | Webb and Sali, 2014 | https://salilab.org/modeller |
| PHENIX | Adams et al., 2010 | https://www.phenix-online.org |
| Sfall | Ten Eyck, 1977 | http://www.ccp4.ac.uk/html/sfall.html |
| Refmac | Brown et al., 2015; Murshudov et al., 1997 | http://www.ccp4.ac.uk/html/refmac5.html |
| Blocres | Heymann and Belnap, 2007 | https://lsbr.niams.nih.gov/bsoft/programs/blocres.html |
| MolProbity | Chen et al., 2010; Davis et al., 2007 | http://molprobity.biochem.duke.edu |
| Chimera | Pettersen et al., 2004 | https://www.cgl.ucsf.edu/chimera |
| Pymol | PyMOL | http://www.pymol.org |
| HOLE | Smart et al., 1996 | http://www.holeprogram.org |
| ClustalX | Larkin et al., 2007 | http://www.clustal.org/clustal2/ |
| Consurf | Ashkenazy et al., 2016 | http://consurftest.tau.ac.il |
| GraphPad Prism 6 | GraphPad Software | http://www.graphpad.com |
| Single-channel kinetic analysis | Csanády, 2000 | http://www.sciencedirect.com/science/article/pii/S0006349500766367 |
| Pclamp9 | Molecular Devices | http://mdc.custhelp.com/app/answers/detail/a_id/18826/~/axon™-pclamp®-9-electrophysiology-data-acquisition-%26-analysis-software-download |
| Other | | |
| R1.2/1.3 400 mesh Au holey carbon grids | Quantifoil | 1210627 |

## CONTACT FOR REAGENT AND RESOURCE SHARING

Requests regarding reagents and further information may be addressed to the Lead Contact, Jue Chen (juechen@rockefeller.edu).

## EXPERIMENTAL MODEL AND SUBJECT DETAILS

### Cell Culture

Insect cells were cultured in sf-900 II SFM medium (GIBCO) supplemented with 5% FBS and 1% Anti-Anti. Freestyle 293 (GIBCO) supplemented with 2% FBS and 1% Anti-Anti was used for mammalian cells. Insect cells were maintained at 28°C and mammalian cells were maintained at 37°C with 8% $CO_2$ and 80% humidity.

### Isolation and injection of *Xenopus laevis* oocytes

*Xenopus laevis* oocytes were removed from anesthesized frogs by ovarian dissection following a IACUC-approved protocol, and the follicular layer removed by collagenase treatment. Oocytes injected with cRNA were incubated at 18°C in a modified Ringer's solution supplemented with 1.8 mM $CaCl_2$ and 50 μg/ml gentamycin.

## METHOD DETAILS

### Expression and Purification of Protein

Human CFTR was expressed and purified with a process similar to that described for zebrafish CFTR (Zhang and Chen, 2016). Briefly, human CFTR gene with a C-terminal GFP tag was cloned into a BacMam expression vector. Human CFTR protein was expressed in

HEK293S GnTI$^-$ cells after baculovirus transduction (Goehring et al., 2014). To purify the protein, cells were first solubilized in lysis buffer (20 mM Tris-HCl pH 7.5, 2 mM $MgCl_2$, 200 mM NaCl, 20% glycerol, and 2 mM DTT) with detergent (1% 2,2-didecylpropane-1,3-bis-β-D-maltopyranoside (LMNG), 0.2% cholesteryl hemisuccinate (CHS), protease inhibitors (1 μg/ml Leupeptin, 1 μg/ml Pepstatin, 1 μg/ml Aprotonin, 100 μg/ml Trypsin inhibitor, 1 mM Benzamidine, and 1 mM PMSF), and DNase I (3 μg/ml) for 2 hr at 4°C. The supernatant was collected after centrifugation at 75,000 g for 1 hr. GFP nanobody (GFPnb) coupled CNBR-activated Sepharose beads (GE Healthcare) were used to affinity purify the protein. GFPnb beads were washed with buffer A (20 mM Tris-HCl pH 7.5, 200 mM NaCl, 2 mM DTT, 2 mM $MgCl_2$, and 0.06% digitonin). The protein was eluted with buffer A after incubation with PreScission protease (10:1 w/w ratio) overnight and was further purified by size exclusion chromatography using a Superose 6 10/300 column (GE Healthcare).

### ATPase Activity Assay

The ATPase activity was measured using an ATP regeneration-NADH consumption coupled system (Scharschmidt et al., 1979). Pyruvate kinase (PK), lactate dehydrogenase (LDH), NADH, and phosphoenolpyruvate (PEP) were purchased from Roche. Purified CFTR was treated with lambda PP (NEB) or PKA (NEB) for 1 hr followed by gel filtration to remove excess ATP and enzyme. The reaction was carried out in a reaction buffer (50 mM HEPES pH 8.0, 150 mM KCl, 0.06% digitonin, 2 mM DTT, 2 mM $MgCl_2$) containing 60 μg/ml of PK, 32 μg/ml LDH, 4 mM PEP, and 0.15 mM NADH. Because of the light sensitivity of NADH, the reaction buffer was kept in the dark before the assay was initiated. Reaction was carried out in 30 μl aliquots in triplicate with a final CFTR concentration of 0.2 μM and different concentrations of $MgCl_2$/ATP. NADH fluorescence depletion was recorded continuously for 45 min by an Infinite M1000 Microplate Reader (TECAN) with excitation wavelength of 340 nm and emission wavelength of 445 nm.

### Electrophysiology

Human CFTR cDNA (pGEMHE-CFTR) was transcribed in vitro using T7 polymerase (Ambion, mMessage T7), and 0.1-10 ng cRNA were injected into *Xenopus laevis* oocytes. Current recordings were made at 25°C in inside-out patches excised from the oocytes 1-3 days after injection.

Patch pipette solution contained (in mM): 136 NMDG-Cl, 2 $MgCl_2$, 5 HEPES, pH 7.4 with NMDG. The continuously flowing bath solution could be exchanged with a time constant < 100 ms, and contained (in mM): 134 NMDG-Cl, 2 $MgCl_2$, 5 HEPES, 0.5 EGTA, pH 7.1 with NMDG. MgATP (2 mM) was added from a 400-mM aqueous stock solution (pH 7.1 with NMDG). 300 nM catalytic subunit of PKA (Sigma) was applied to activate CFTR channels. Macroscopic and unitary currents were recorded at a membrane potential of −80 mV (Axopatch 200B, Molecular devices), filtered at 2 kHz, and digitized at 10 kHz.

Single-channel patches were identified from long (typically 10 min) recordings without superimposed channel openings. To reconstruct open bursts and interbursts, of durations $\tau_b$ and $\tau_{ib}$ respectively, currents from patches containing no superimposed channel openings were baseline subtracted to remove slow drifts, refiltered at 100 Hz, and idealized by half-amplitude threshold crossing. After imposition of a fixed dead time of 4 ms, the resulting events lists were subjected to kinetic analysis as described (Csanády et al., 2000). Open bursts were isolated by suppressing brief closures shorter than a cutoff estimated using the method of Magleby and Pallotta (Magleby and Pallotta, 1983), as described (Csanády et al., 2010).

Macroscopic current activation time courses were fit to a two-step two-parameter activation scheme, D- > P- > M, using non-linear least-squares methods (pCLAMP 9, Molecular Devices), yielding net sequential activation rates, $k_{a1}$ and $k_{a2}$ (Figure 5B).

### EM Sample Preparation and Data collection

The purified human CFTR sample was concentrated to 5.5 mg/ml and supplemented with 3 mM fluorinated Fos-Choline-8. Three μl of the protein sample was applied to each Quantifoil R1.2/1.3 400 mesh Au holey carbon grid (Quantifoil), blotted with Vitrobot Mark IV (FEI) for 3 s at blot force 0 after 15 s wait time, and frozen in liquid ethane. A 300 kV Titan Krios (FEI) with a Gatan K2 Summit direct electron detector (Gatan) was used to image the grids. Images were recorded by Serial EM in super-resolution mode with a pixel size of 0.4085 Å/pixel. For data collection, each image was exposed for 7 s in 50 subframes with a dose rate of 8 electrons per pixel per second. A defocus range from −0.8 μm to −2.5 μm was used.

### Imaging Processing and 3D reconstruction

Dark subtracted images were first normalized by gain reference and binned by 2x, resulting in a pixel size of 0.817 Å/pixel. Drift correction was performed using the program Unblur (Grant and Grigorieff, 2015). The contrast transfer function (CTF) was estimated using CTFFIND4 (Rohou and Grigorieff, 2015). To generate templates for automatic picking, around 5000 particles were manually picked and classified by 2D classification in RELION (Scheres, 2012). After automatic picking and manual micrograph inspection, 415,915 particles were extracted for subsequent 2D and 3D classification. Motion correction of individual particles was performed using the program alignparts_lmbfgs (Rubinstein and Brubaker, 2015). Using the structure of zebrafish CFTR (PDB: 5UAR) low pass filtered to 60 Å as the initial model, 3D classification was carried out in RELION (Scheres, 2012). The best class, containing 33% of the particles, gave rise to an 8.26 Å map. The refinement was performed in FREALIGN (Grigorieff, 2016) using this best class as the initial model and all particles post motion correction to generate the final map for model construction.

### Model Construction

To get better side chain densities for model building, we sharpened one half-map using BFACTOR.EXE (author: Nikolaus Grigorieff) with a resolution limit of 3.9 Å and a b-factor value of −250 Å$^2$. To build TMD1 and TMD2 (residues 5-389 and 844-1172), we first generated a model based on the structure of zebrafish CFTR (PDB: 5UAR) using the program Modeler (Webb and Sali, 2014), then fitted and rebuilt the model into the cryo-EM map in COOT (Emsley et al., 2010). For the NBDs, the crystal structures of human NBD1 (PDB: 2PZG) and human NBD2 (PDB: 3GD7) were used as initial models. For regions with good densities, the residues were adjusted based on the map. For regions with weak densities, the residues were kept as they were in the models. The overall densities for the R domain were too weak to build; however, the C-terminal region of the R domain, which connects to elbow helix 2 of TMD2, had continuous densities. Based on the secondary structure prediction by Phyre2 (Kelley et al., 2015), this region contains an α-helix (residues 830-841). Therefore, we modeled a poly-alanine helix into the tubular density. The final structure includes residues 5-389 of TMD1; 390-402 and 439-645 of NBD1; 844-883 and 909-1172 of TMD2; 1207-1436 of NBD2; and 19 alanines that likely correspond to residues 825-843 of the R domain.

### Model Refinement and Validation

The model was refined in real space using PHENIX (Adams et al., 2010) and also in reciprocal space using Refmac (Brown et al., 2015; Murshudov et al., 1997). Structural factors were calculated from a half-map (working) using the program Sfall (Ten Eyck, 1977). The R work and R free values were calculated with a mask containing the model plus a 2Å margin. Fourier shell correlations (FSCs) were calculated between the two half maps, the model against the working map, the other (free) half map, and full (sum) map (Scheres and Chen, 2012; Wang et al., 2014). Local resolutions were estimated using Blocres (Heymann and Belnap, 2007). MolProbity (Chen et al., 2010; Davis et al., 2007) was used to validate the geometries of the model.

Structure figures were genereated using Pymol (http://www.pymol.org), Chimera (Pettersen et al., 2004), and HOLE (Smart et al., 1996).

### Sequence conservation analysis

Sequence alignments were carried out in ClustalX (Larkin et al., 2007) and the conservation analysis was performed using the ConSurf Server (Ashkenazy et al., 2016).

## QUANTIFICATION AND STATISTICAL ANALYSIS

GraphPad Prism 6 was used to fit the Michaelis-Menten curve of ATPase activity and to calculate Km and Vmax. The goodness of fit was represented by R square values (phosphorylated protein has an R square of 0.95 and dephosphorylated protein has an R square of 0.84).

All electrophysiological kinetic parameters are given as mean ± SEM extracted from n = 9 and 11 recordings, respectively, of single-channel and macroscopic currents.

## DATA AND SOFTWARE AVAILABILITY

The accession numbers for the structure reported in this paper are PDB: 5UAK and EMD: EMD-8516.

Cell

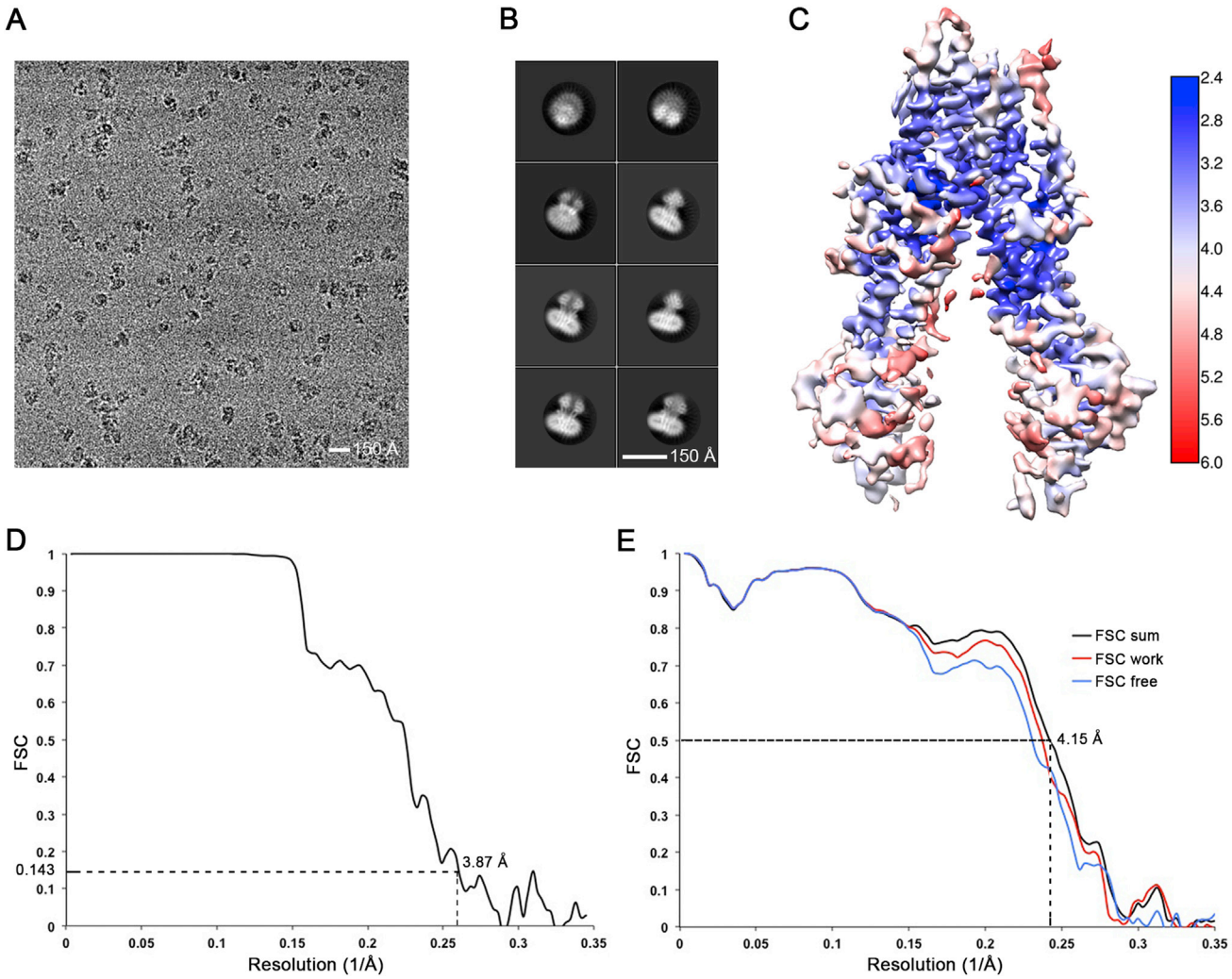


**Figure S1. Cryo-EM Analysis, Related to Figure 1**

(A) A representative micrograph at defocus of −2.3 μm.

(B) Representative 2D class averages, output of Relion (Scheres, 2012).

(C) The overall EM map colored by local resolution estimation using Blocres (Heymann and Belnap, 2007).

(D) Fourier Shell Correlation (FSC) as a function of resolution, using Frealign (Grigorieff, 2016) output.

(E) FSC calculated between the refined structure and three different maps. Black: the map calculated using the full dataset (sum); Red: the half map used in refinement (work); Blue: the other half map (free).

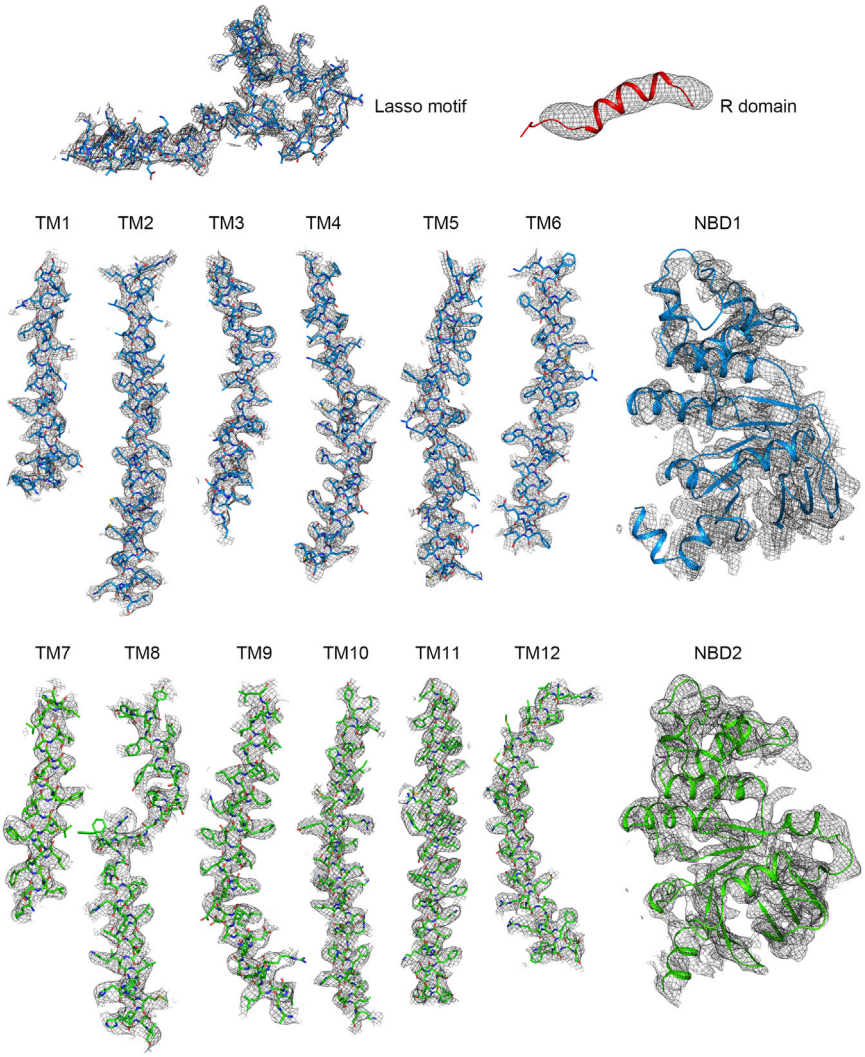


**Figure S2. EM Density of Different Parts of the Structure, Related to Figure 1**

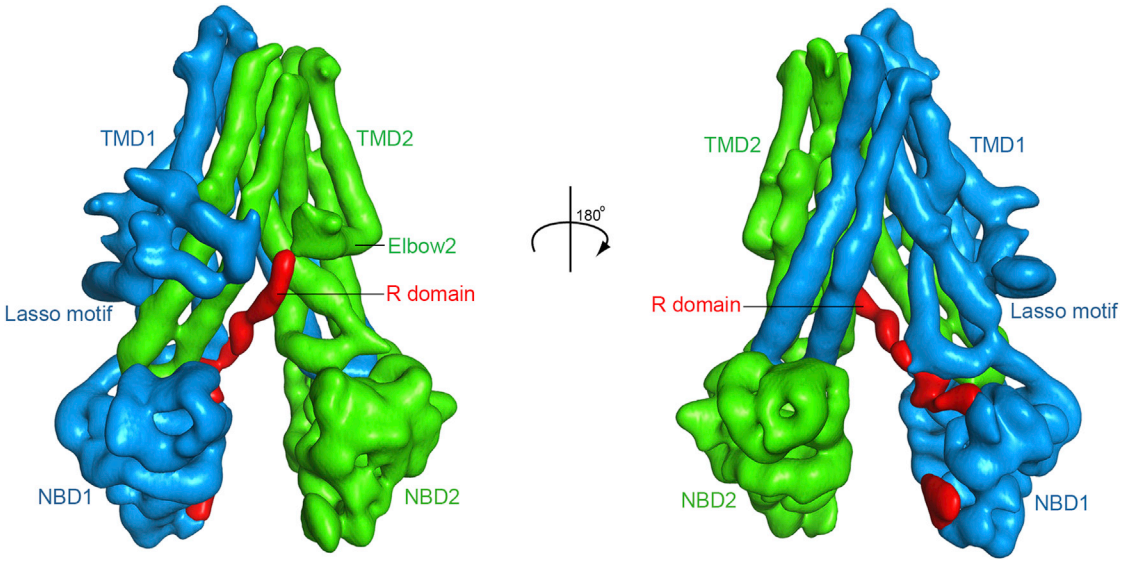


**Figure S3. The Cryo-EM Map of CFTR without B-Factor Sharpening, Related to Figures 1 and 4**

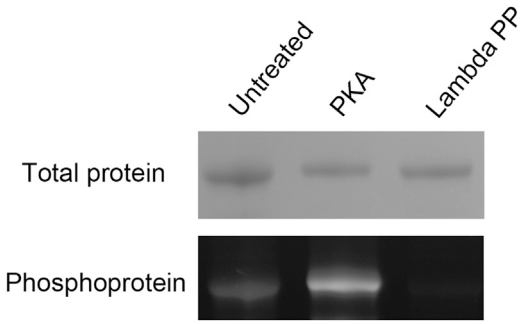


**Figure S4. Analysis of the Phosphorylation State of Purified CFTR, Related to Figure 5**

Untreated, PKA-treated, and Lambda Protein Phosphatase (PP)-treated samples on SDS-PAGE were stained by Coomassie blue (upper) and the Pro-Q Diamond Phosphoprotein Gel Stain (lower).